Article

Antiferromagnetic quantum anomalous Hall effect under spin flips and flops

https://doi.org/10.1038/s41586-025-08860-z

Received: 20 August 2024

Accepted: 4 March 2025

Published online: 16 April 2025

Check for updates

Zichen Lian[1,8], Yongchao Wang[1,8], Yongqian Wang[2,3], Wen-Han Dong[1], Yang Feng[4], Zehao Dong[1], Mangyuan Ma[1], Shuai Yang[2,3], Liangcai Xu[1], Yaoxin Li[1], Bohan Fu[2,3], Yuetan Li[1], Wanjun Jiang[1], Yong Xu[1,5,6], Chang Liu[2,3] ✉, Jinsong Zhang[1,7] ✉ & Yayu Wang[1,5,7] ✉

The interplay between nontrivial band topology and layered antiferromagnetism in $MnBi_2Te_4$ has opened a new avenue for exploring topological phases of matter[1–4]. The quantum anomalous Hall effect[5] and axion insulator state[6] have been observed in odd and even number layers of $MnBi_2Te_4$, and the quantum metric nonlinear Hall effect[7,8] has been shown to exist in this topological antiferromagnet. The rich and complex antiferromagnetic spin dynamics in $MnBi_2Te_4$ is expected to generate new quantum anomalous Hall phenomena that are absent in conventional ferromagnetic topological insulators, but experimental observations are still unknown. Here we fabricate a device of 7-septuple-layer $MnBi_2Te_4$ covered with an AlO_x capping layer, which enables the investigation of antiferromagnetic quantum anomalous Hall effect over wide parameter spaces. By tuning the gate voltage and perpendicular magnetic field, we uncover a cascade of quantum phase transitions that can be attributed to the influence of complex spin configurations on edge state transport. Furthermore, we find that an in-plane magnetic field enhances both the coercive field and the exchange gap of the surface state, in contrast to that in the ferromagnetic quantum anomalous Hall state. Combined with numerical simulations, we propose that these peculiar features arise from the spin flip and flop transitions that are inherent to a van der Waals antiferromagnet. The versatile tunability of the quantum anomalous Hall effect in $MnBi_2Te_4$ paves the way for potential applications in topological antiferromagnetic spintronics[9,10].

The quantum anomalous Hall (QAH) effect realizes one-dimensional dissipationless chiral edge state transport in the absence of external magnetic field[11]. Over the past decade, the pursuit of new materials exhibiting the QAH effect with new types of quantization has been a rapidly developing field[5,11–19]. Among the various systems explored, only $MnBi_2Te_4$ hosts the QAH effect in the presence of bulk antiferromagnetic (AFM) order, thus can be dubbed the AFM QAH state. As shown in Fig. 1a, the Mn moments in each septuple layer (SL) exhibit intralayer ferromagnetic order, but AFM order between neighbouring SLs[1–3,6,20–24]. As proposed theoretically, different spin stacking sequences of the SLs and various metamagnetic phases will lead to fundamentally different bulk band topology and edge state conduction[25–28]. Recently, even–odd layer-dependent magnetism and the long-sought surface spin flop (SSF) transition have been observed in $MnBi_2Te_4$ (refs. 29–31), which triggered the search for new QAH behaviour modulated by spin configurational variations. However, there has been limited experimental progress along this direction, mainly owing to the technical challenges in obtaining high-quality devices with zero-field quantization[5]. It has been shown that the $MnBi_2Te_4$ crystals are prone to various types of defect[32–39], and the nano-fabrication process for transport device may introduce further complications[40].

In this work, we design a new device architecture based on 7-SL $MnBi_2Te_4$, in which markedly improved quantum transport performance can be achieved. The $MnBi_2Te_4$ single crystal is grown by solid-state reaction, and its high Néel temperature $T_N \approx 26$ K indicates high crystalline quality (see Supplementary Figs. 1–3 for the calibrations of bulk crystal). We notice that in most odd-number-SL $MnBi_2Te_4$ devices exhibiting a large anomalous Hall effect (AHE), one surface of the thin film is in contact with AlO_x, either as the exfoliation agent[5,41] or as epitaxial substrate[42,43]. This suggests that AlO_x may play an important part in enhancing the AHE in this system, most likely by stabilizing the surface out-of-plane magnetic order. The enhancement of perpendicular magnetic anisotropy (PMA) has been frequently observed in spintronic material systems, such as Pt/Co/AlO_x (refs. 44–47). Our first-principles calculations also demonstrate an enhancement of surface PMA for $MnBi_2Te_4$ covered with AlO_x, primarily because of the hole doping and strong spin–orbit coupling of Te atoms (Supplementary Information section B). We implement this idea by depositing an AlO_x capping layer on the exfoliated $MnBi_2Te_4$ flake before performing

[1]State Key Laboratory of Low Dimensional Quantum Physics, Department of Physics, Tsinghua University, Beijing, People's Republic of China. [2]School of Physics, Renmin University of China, Beijing, People's Republic of China. [3]Key Laboratory of Quantum State Construction and Manipulation (Ministry of Education), Renmin University of China, Beijing, People's Republic of China. [4]Beijing Academy of Quantum Information Sciences, Beijing, People's Republic of China. [5]New Cornerstone Science Laboratory, Frontier Science Center for Quantum Information, Beijing, People's Republic of China. [6]RIKEN Center for Emergent Matter Science (CEMS), Wako, Japan. [7]Hefei National Laboratory, Hefei, China. [8]These authors contributed equally: Zichen Lian, Yongchao Wang. ✉e-mail: liuchang_phy@ruc.edu.cn; jinsongzhang@tsinghua.edu.cn; yayuwang@tsinghua.edu.cn

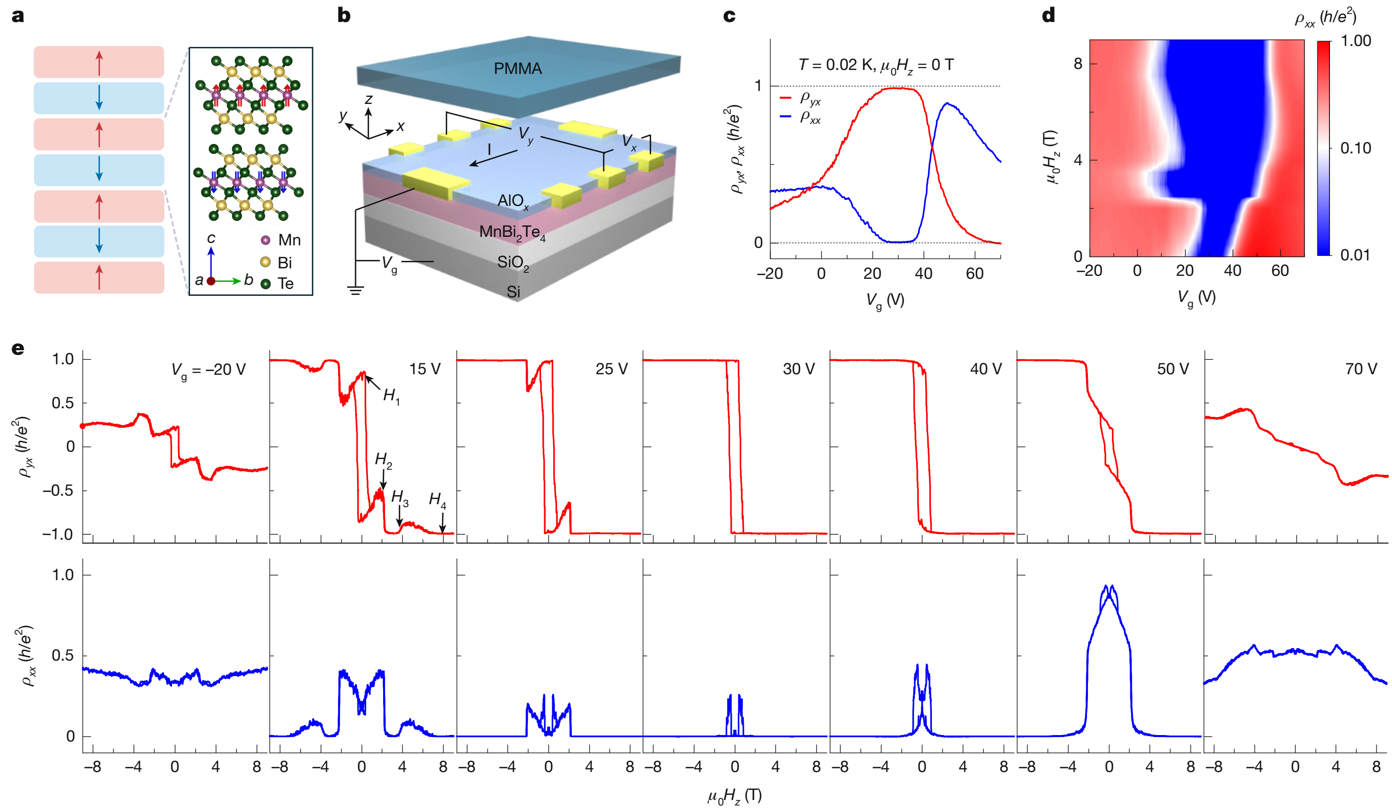

Fig. 1 | Crystal structure, device configuration and V_g-dependent transport of 7-SL $MnBi_2Te_4$. **a**, Schematic crystal structure of $MnBi_2Te_4$. The red and blue arrows indicate the direction of magnetic moments of Mn ions in different SLs. **b**, Schematic transport configuration of a 7-SL $MnBi_2Te_4$ flake on a SiO_2/Si substrate. The top surface of $MnBi_2Te_4$ is covered with a 3-nm AlO_x capping layer. **c**, V_g-dependent ρ_{yx} and ρ_{xx} at $\mu_0H_z = 0$ T and $T = 0.02$ K. The QAH effect appears at the CNP around $V_g = 30$ V. **d**, Colour map of ρ_{xx} as a function of V_g and H_z. The blue region represents the area of the QAH state. **e**, H_z dependence of ρ_{xx} and ρ_{yx} at various V_gs at $T = 0.02$ K. The arrows in the $V_g = 15$ V panel indicate the four characteristic field scales of the cascaded quantum phase transitions.

spin-coating of polymethyl methacrylate (PMMA), as schematically shown in Fig. 1b (see Methods for details). The AlO_x layer also protects against the environmental contamination and damage from the fabrication process[40], which is detrimental to the QAH effect. The other side of the flake directly lies on the SiO_2/Si substrate, which also serves as a bottom-gate dielectric.

Cascade of quantum phase transitions in AFM QAH effect

Our device architecture enables the investigation of the AFM QAH effect over a wide range of control parameters, including gate voltage (V_g), temperature (T), perpendicular and in-plane magnetic fields. Figure 1c presents the V_g-dependent Hall resistivity (ρ_{yx}) and longitudinal resistivity (ρ_{xx}) measured at $T = 0.02$ K in zero perpendicular magnetic field $\mu_0H_z = 0$ T. The quantized ρ_{yx} and vanishing ρ_{xx} at the charge neutrality point (CNP) around $V_g = 30$ V demonstrate the dissipationless nature of the chiral edge state in the QAH phase. To map out the full phase diagram, we sweep V_g at different fixed H_z values. Figure 1d shows the colour map of ρ_{xx} as a function of V_g and H_z, in which the blue region with small ρ_{xx} represents the QAH state (see Extended Data Fig. 1 for the ρ_{yx} map and transport results for different H_z). The QAH region expands suddenly as μ_0H_z increases to around 2.2 T, especially for the hole-doped side ($V_g < 30$ V) that was unexplored before[5]. The QAH region then shrinks abruptly near 3.8 T, and after that broadens gradually with increasing H_z. Compared with that in the ferromagnetic topological insulator systems[11,48–50], the AFM QAH state here demonstrates a much richer response to variations in V_g and H_z.

To illustrate the quantum transport more clearly, in Fig. 1e we show the H_z-dependent ρ_{yx} and ρ_{xx} loops at $T = 0.02$ K for representative V_gs. At $V_g = 30$ V, the sample exhibits the anticipated QAH effect with ρ_{yx} being nearly quantized at $0.981h/e^2$, and ρ_{xx} dropped to $0.011h/e^2$ at $\mu_0H_z = 0$ T. At $\mu_0H_1 \approx 0.5$ T, there is a sharp plateau transition corresponding to the sign reversal of the Chern number from $C = +1$ to -1. Above that, ρ_{yx} remains at the quantized plateau because for a narrow range of $V_g \approx 30$ V the QAH state persists over the entire H_z regime, which can be visualized as a vertical linecut in Fig. 1d. When V_g deviates from the CNP, we first observe a linear behaviour of ρ_{yx} at low H_z, indicating that hole- ($V_g \leq 25$ V) and electron-type ($V_g \geq 40$ V) carriers begin to contribute to the ordinary Hall effect. With varied V_g and H_z, a cascade of quantum phase transitions characterized by the deviation and recovery of ρ_{yx} quantization start to emerge, especially in the hole-doped regime that was unexplored before[5]. As indicated by the arrows in the $V_g = 15$ V panel, at $\mu_0H_2 \approx 2.2$ T the ρ_{yx} shows a sudden jump and returns to the $-h/e^2$ plateau, meanwhile ρ_{xx} drops from a finite value to nearly zero. The quantized state is maintained until $\mu_0H_3 \approx 3.8$ T, above which it is suppressed into a broad region with pronounced dissipation. When the magnetic field exceeds $\mu_0H_4 \approx 7.8$ T, the quantized ρ_{yx} plateau and vanishing ρ_{xx} are restored and strengthened.

We then study the T evolution of the ρ_{yx} and ρ_{xx} loops at $V_g = 30$ V, as shown in Fig. 2a (see Extended Data Fig. 2 for separately displayed curves). In contrast to the quantized ρ_{yx} plateau persisting over the entire H_z range at $T = 0.02$ K, the high-T curves exhibit much more complex variations that resonate with the cascaded V_g evolution at the ground state. Most of the curves exhibit four characteristic H_z scales, namely, the ρ_{yx} sign reversal at H_1, the sudden increase in ρ_{yx} at H_2, the weakening of ρ_{yx} at H_3, and the recovery of ρ_{yx} plateau above H_4. To directly visualize the T-dependent phase transitions, we plot the variation of ρ_{yx} and its derivative versus H_z in the T–H_z plane, as shown by the coloured maps in Fig. 2b,c. Here the four white dashed lines represent

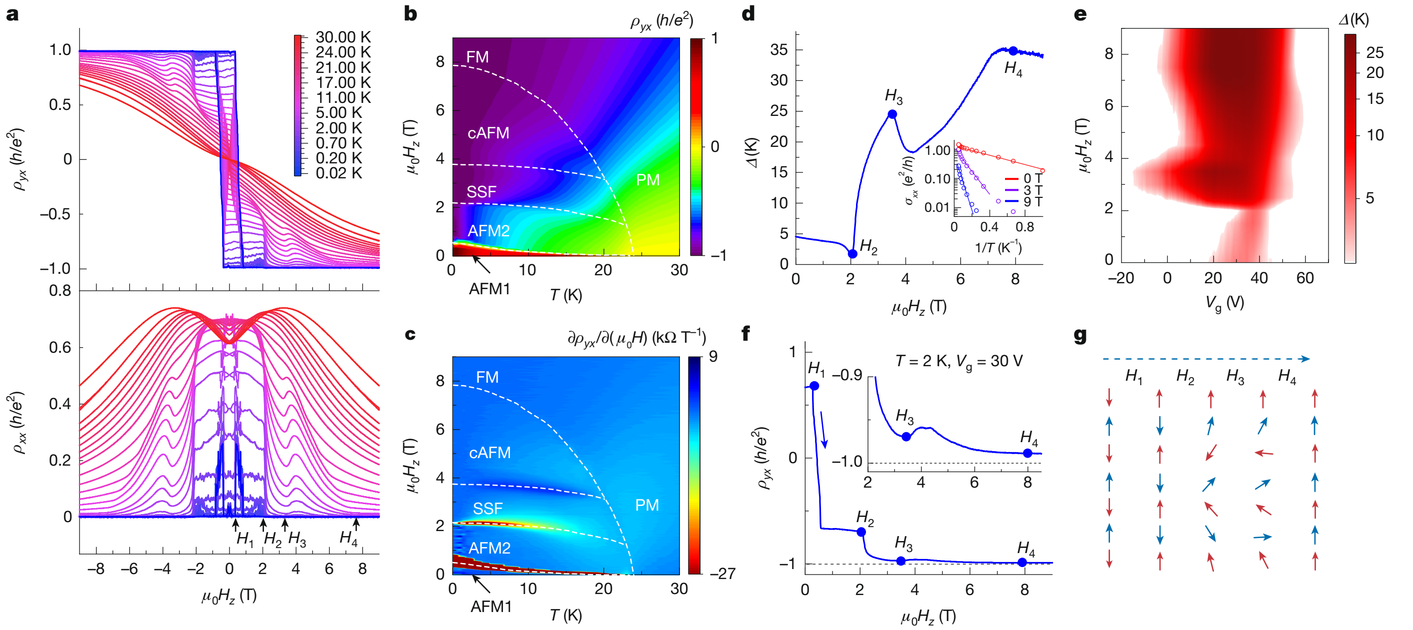

Fig. 2 | T dependence of transport properties at V_g = 30 V and thermally activated gap fitting at varied μ_0H_z. **a**, H_z-dependent ρ_{yx} and ρ_{xx} loops at selected temperatures at V_g = 30 V. **b**,**c**, Colour maps of ρ_{yx} and $\partial\rho_{yx}/\partial H_z$. The phase diagram is separated into the AFM1, AFM2, SSF, cAFM, ferromagnetic (FM) and paramagnetic (PM) regions by four characteristic field scales (H_1, H_2, H_3, H_4) marked by white dashed lines. **d**, The thermal activation gap size Δ as a function of H_z. The inset shows the Arrhenius plots of σ_{xx} at μ_0H_z = 0, 3, and 9 T. **e**, Colour map of Δ as a function of H_z and V_g. **f**, Evolution of ρ_{yx} with μ_0H_z at T = 2 K, which shows a one-to-one correspondence between the ρ_{yx} transitions and changes of Δ. **g**, Schematic magnetic configurations for the 7-SL device for varied H_z.

the characteristic H_z scales that separate the phase diagram into several distinct regions, and the nature of each phase will be discussed later.

Spin flips and flops in the van der Waals AFM state

To quantitatively characterize the robustness of each quantized state, we perform the Arrhenius fitting on the longitudinal conductivity σ_{xx} versus T to extract the thermal activation gap size Δ around the Dirac point of the surface state. The complete colour maps of σ_{xx} as a function of T and V_g at various μ_0H_z are presented in Extended Data Fig. 3. As shown in the Fig. 2d (inset), log(σ_{xx}) exhibits a linear dependence on 1/T, indicating a thermal activation behaviour $\sigma_{xx} \propto \exp(-\Delta/2k_BT)$. Figure 2d shows the evolution of Δ as a function of H_z at V_g = 30 V. The most dramatic feature is the abrupt jump of Δ at $\mu_0H_2 \approx 2.2$ T, after which Δ/k_B increases from about 4 K to near 25 K. Above $\mu_0H_3 \approx 3.8$ T, it begins to decrease, reaches a minimum and increases again up to around 35 K at $\mu_0H_4 \approx 7.8$ T. Figure 2f and its inset show the H_z dependence of ρ_{yx} at T = 2 K, which shows a one-to-one correspondence between the ρ_{yx} transitions and Δ variations. Figure 2e shows the mapping of Δ with H_z under different V_gs, which exhibits a similar pattern as the ρ_{xx} map in Fig. 1d.

The H_z-dependent gap size helps to identify the corresponding magnetic order of each state. By performing a simulation based on the modified AFM spin chain model[29,31,51–53], in conjunction with previous results, we derive the magnetic configurations schematically shown in Fig. 2g (see Supplementary Fig. 9 for details). The evolution of magnetic configuration in H_z plays an important part in the electronic band structure, as well as the quantized transport. First-principles calculation for the band structure of these noncolinear metamagnetic states is a formidable task, but we can gain more insights about the relationship between spin configuration and electronic structure utilizing the coupled Dirac cone model for possible collinear ground states[26]. As shown in Supplementary Information section D, we demonstrate that the Δ value is determined mainly by the perpendicular magnetization of the surface and subsurface SLs. Therefore, the measured gap size provides an important clue about the spin orientations of the surface and subsurface layers, which overcomes the limitation of previous magnetic measurements that detect only the overall magnetization[29–31,54]. Below we describe the magnetic order and corresponding gap size for each phase.

The transition at H_1 is because of the spin flip from the ↓↑↓↑↓↑↓ (AFM1) state to the ↑↓↑↓↑↓↑ (AFM2) state, where ↑ and ↓ represent the magnetization of each SL. This spin flip leads to the switch of Chern number between ±1 but Δ remains intact. Above H_4, the magnetic moments in all SLs are polarized into the ferromagnetic state, leading to a robust Chern insulator phase with large Δ. The slow suppression of Δ at even higher H_z can be attributed to the opposite sign of the internal exchange field in $MnBi_2Te_4$ to the external H_z, as shown in previous experiments[5,55]. The $\mu_0H_3 \approx 3.8$ T field scale coincides with the bulk spin flop transition that has been demonstrated by polar reflective magnetic circular dichroism (RMCD)[29,31], after which all SLs enter the canted AFM (cAFM) state that can exhibit the QAH effect in thin flakes[22]. During this process, the z-component of bulk magnetization increases with H_z but is reduced at the bottom SL, leading to a slightly decreased gap size[29]. This is consistent with the trend shown in Supplementary Information section D that the perpendicular magnetization near the surface plays a much more important part in determining Δ than the bulk magnetization. The $\mu_0H_2 \approx 2.2$ T transition is the most puzzling one, which causes a marked increase in Δ. We note that this field scale is very close to the SSF transition in 6-SL $MnBi_2Te_4$ with bare top surface[29,31,54], which should be absent in odd-SL devices. In our 7-SL device, the strong bonding of the top SL with the AlO_x capping layer may induce much stronger PMA and much weaker AFM coupling with the subsurface layer[53]. At H_2, the bottom 6-SL block undergoes a SSF transition, similar to that revealed by RMCD measurement and theoretical calculation[29]. After that, the subsurface SL is flopped to nearly parallel to the top SL, and the bottom SL keeps an out-of-plane magnetization. This magnetic configuration is highly beneficial for the QAH effect because of the enhancement of near-surface magnetization[26,27], leading to the significant increase of Δ.

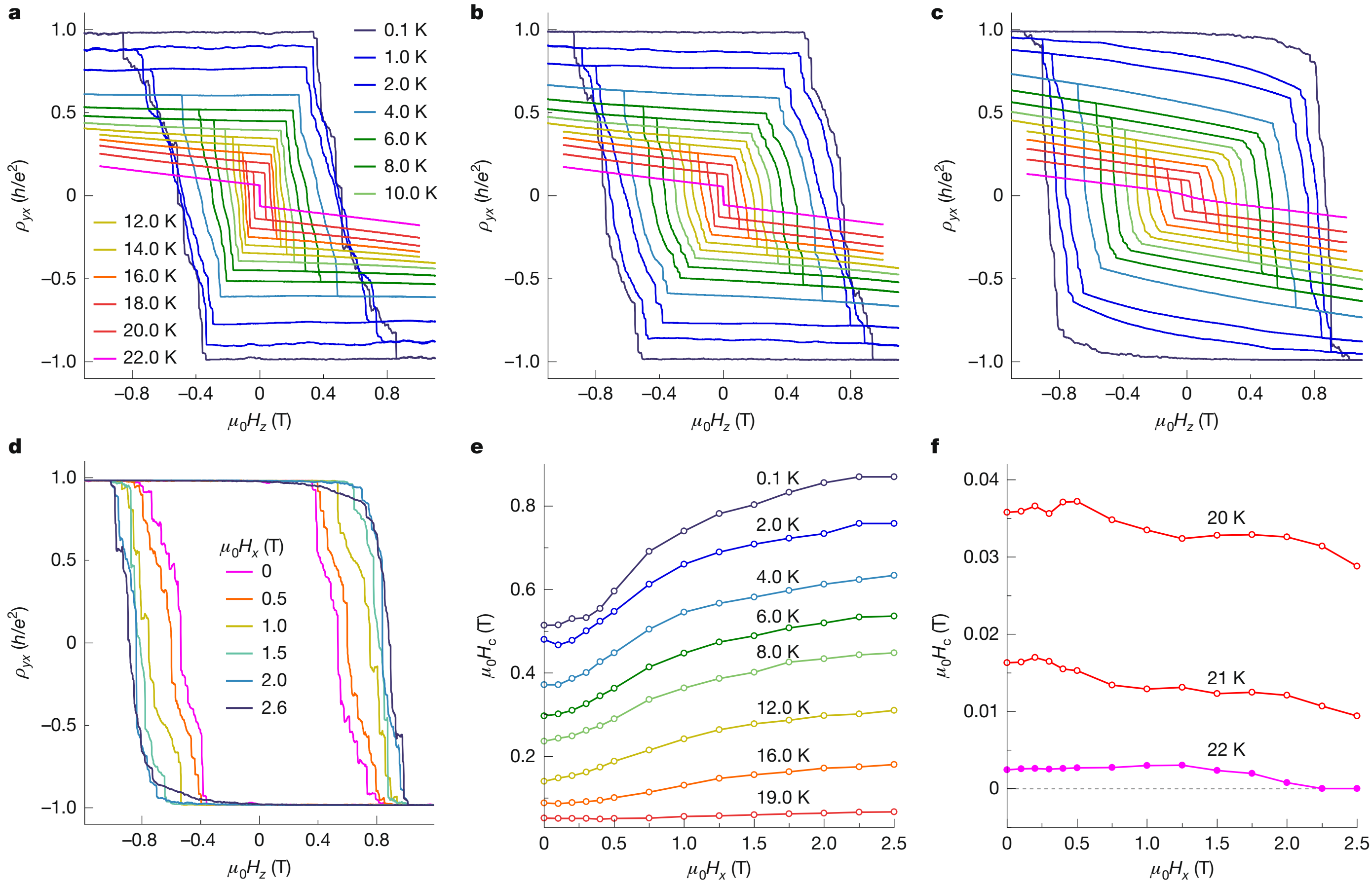

Fig. 3 | Enhancement of the hysteresis by an in-plane magnetic field. **a**–**c**, Evolution of H_z-dependent ρ_{yx} loops with T at in-plane magnetic field $\mu_0H_x = 0$ T (**a**), 1 T (**b**) and 2.5 T (**c**). In each panel, the loop shrinks with increasing T, but overall they become wider with increasing H_x. **d**, The μ_0H_z-dependent ρ_{yx} loops at $T = 0.02$ K for varied μ_0H_x, directly showing the enhancement of hysteresis by in-plane magnetic field. **e**,**f**, The coercive field H_c as a function of H_x for various Ts. It increases with H_x up to 19 K (**e**), but above that the trend reverses (**f**).

Anomalous influence of the in-plane magnetic field

Now the spin configuration of each phase is clarified, we use another tuning parameter, the in-plane magnetic field H_x, to manipulate the magnetic order and quantum transport phenomena. Figure 3–c shows the T evolution of ρ_{yx} versus H_z loops measured at $V_g = 30$ V under selected H_x values. In each panel, the hysteresis loops shrink with increasing T (the complete dataset is shown in Extended Data Figs. 4 and 5), just as expected. However, for the same T in the low T regime, the hysteresis loops expand with increasing H_x, indicating the enhancement of coercivity. This trend can be directly illustrated by comparing the hysteresis loops in varied H_x at $T = 0.02$ K, as shown in Fig. 3d. The enhancement of hysteresis becomes weaker and exhibits an opposite trend at higher T, and the coercive loop at 22 K is completely suppressed by a sufficiently large H_x. In Fig. 3e,f, we plot the variation of coercive field H_c, defined by the field scale when $\rho_{yx} = 0$, as a function of H_x at different Ts, which demonstrates the two opposite trends in different T regions.

Apart from the enhancement of hysteresis, the in-plane field also strengthens the AFM QAH effect. Figure 4a,b shows the influence of H_x on the ρ_{yx} compared with H_z loops for two regimes in the phase diagram: the hole-doped region ($V_g = 25$ V) at $T = 0.02$ K and the CNP region ($V_g = 30$ V) at $T = 0.7$ K. In the absence of H_x, both regimes have weakened QAH effect with nonquantized ρ_{yx} between H_1 and H_2. As H_x increases, in both cases ρ_{yx} is enhanced to form a well-developed quantum plateau and the transition near H_2 becomes smoother. Figure 4c,d shows the phase diagrams at $T = 0.02$ K constructed by plotting σ_{xx} in the V_g and H_z plane for $\mu_0H_x = 0$ and 1.5 T, respectively (see Extended Data Fig. 6 for the complete data of σ_{xx} colour map for varied H_x). Notably, the application of H_x enlarges the blue area with dissipationless chiral edge state transport. Figure 4e presents the evolution of Δ in different μ_0H_x values extracted from the temperature dependences (see Extended Data Fig. 7 for the raw data), which demonstrates the increase of Δ and the smoothing of $\mu_0H_2 \approx 2.2$ T transition induced by H_x.

The enhancement of coercivity and QAH effect by an in-plane magnetic field contrasts with that for magnetically doped topological insulators[56]. As shown recently in Cr doped $(Bi,Sb)_2Te_3$ thin films, an in-plane field significantly decreases the H_c and suppresses the zero field ρ_{yx}. Both trends can be explained by the Stoner–Wohlfarth model for coherent rotation[57,58], in which the in-plane field tilts the perpendicular magnetization and reduces the switching barrier. The highly unusual influence of the in-plane magnetic field on the AFM QAH effect in $MnBi_2Te_4$ is against our intuition and must be related to its unique spin dynamics.

Discussion

To explain the enhancement of QAH effect by the in-plane magnetic field, we still resort to the simulation based on the modified AFM spin chain model[29,31,51–53]. The simulation renders a change of spin configuration that can well account for the anomalous behaviour, as shown in Supplementary Fig. 8. The key factors are the AlO_x capping layer and the van der Waals AFM order that are unique to the 7-SL $MnBi_2Te_4$ device studied here. The strong PMA of the top SL and the reduced AFM coupling with the subsurface layer ensures that in the presence of

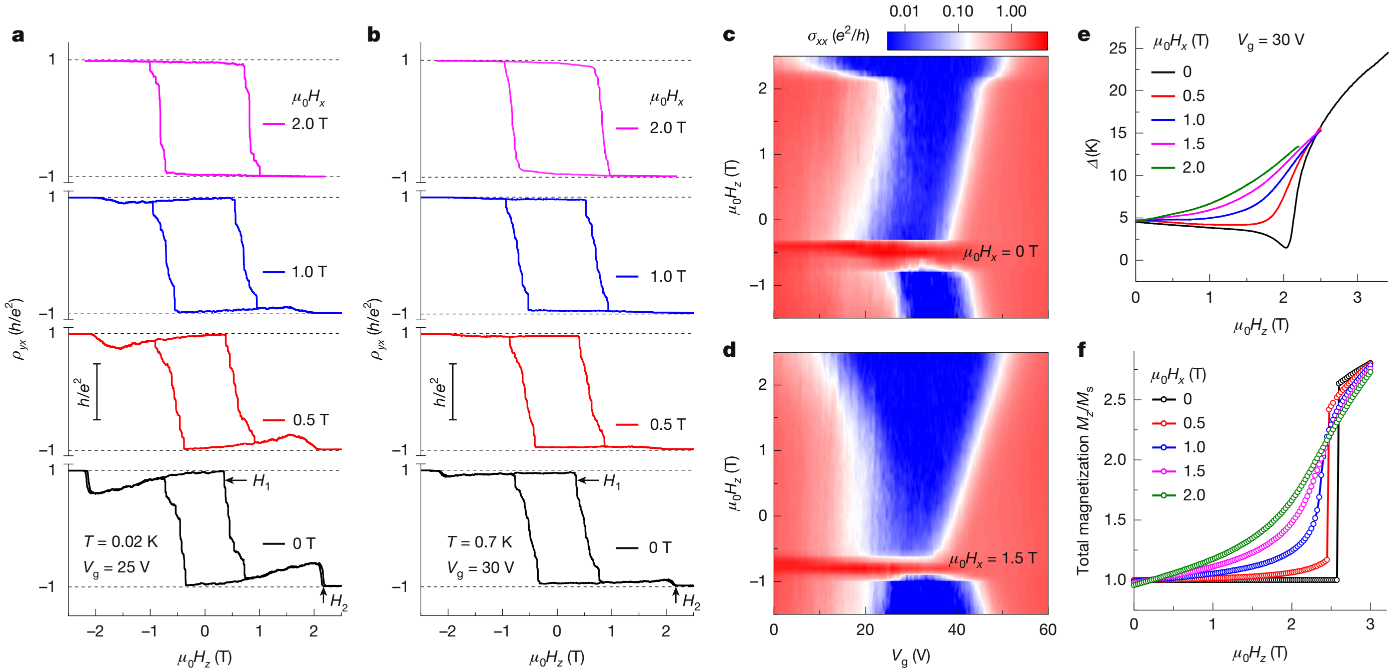

Fig. 4 | The enhancement of QAH effect by an in-plane magnetic field. The μ_0H_z-dependent ρ_{yx} at $V_g = 25$ V and $T = 0.02$ K (**a**), $V_g = 30$ V and $T = 0.7$ K (**b**) in different H_x. In both cases, the QAH state between H_1 and H_2 is enhanced by the in-plane magnetic field. **c**,**d**, The colour map of σ_{xx} as a function of H_z and V_g with $\mu_0H_x = 0$ and 1.5 T, respectively, at $T = 0.02$ K. The blue region characteristic of the QAH state is widened by H_x. **e**, The evolution of extracted Δ with H_z in different H_x. **f**, The simulated total magnetization along the z-axis under different H_x based on a modified AFM spin chain model. It shows similar behaviour as Δ in **e**, indicating the enhancement of QAH effect by in-plane magnetic field.

in-plane magnetic field, the enhancement of z-component magnetization due to the down-moment rotation exceeds the reduction of the z-component due to the up-moment tilting. As shown in Fig. 4f, the total magnetization along the z-axis is enhanced by H_x, especially for SLs near the surface, which facilitates the gap opening at the Dirac point[26,27]. The in-plane magnetic field thus promotes an earlier transition into the SSF state, as demonstrated in both the experiment (Fig. 4e) and the simulation (Fig. 4f), leading to a larger energy gap hence better QAH state.

The increase of H_c by in-plane magnetic field turns out to be a much more complicated problem and cannot be explained simply by the AFM spin chain model or micromagnetic simulations. There are two key differences between the AFM QAH state here and the ferromagnetic QAH state in magnetically doped topological insulators. First, the local moments in $MnBi_2Te_4$ form a regular lattice rather than random spatial distribution. Second, the interlayer exchange is AFM rather than ferromagnetic. The uncompensated spins of the 7-SL $MnBi_2Te_4$ leads to a net magnetization along the z-axis, and the AFM1 to AFM2 transition at H_c corresponds to the coherent flips of all magnetic layers simultaneously because they collectively form the quantum ground state. Therefore, a much more sophisticated model might be needed to describe this phase transition and the enhancement of coercivity by in-plane magnetic field. It has been shown that a transverse field can enhance domain pinning and harden the magnet through site-random fields in a disordered Ising spin chain with ferromagnetic dipole interaction[59,60]. It is interesting to see if this mechanism also applies to the van der Waals AFM order in $MnBi_2Te_4$. At higher T close to T_N, the weakened AFM order and increased thermal fluctuations may drive the system into a classical regime described by the Stoner–Wohlfarth model, in which the in-plane field softens the hysteresis.

The 7-SL $MnBi_2Te_4$ device with an AlO_x capping layer exhibits a cascade of quantum phase transitions induced by the influence of spin flips and flops on the topological transport properties that are unique to the van der Waals layered AFM order. The close correlation between magnetism and band topology also enables us to probe the magnetic order through quantum transport measurements. We find that an in-plane magnetic field enhances both the hysteresis and the energy gap on the topological surface state, in contrast to that in ferromagnetic QAH systems. This powerful in situ knob is crucial for exploring new topological phenomena based on the AFM QAH effect and the application of $MnBi_2Te_4$ in topological AFM spintronics[9,10].

Online content

Any methods, additional references, Nature Portfolio reporting summaries, source data, extended data, supplementary information, acknowledgements, peer review information; details of author contributions and competing interests; and statements of data and code availability are available at https://doi.org/10.1038/s41586-025-08860-z.

1. Otrokov, M. M. et al. Prediction and observation of an antiferromagnetic topological insulator. *Nature* **576**, 416–422 (2019).
2. Gong, Y. et al. Experimental realization of an intrinsic magnetic topological insulator. *Chin. Phys. Lett.* **36**, 076801 (2019).
3. Li, J. et al. Intrinsic magnetic topological insulators in van der Waals layered $MnBi_2Te_4$-family materials. *Sci. Adv.* **5**, eaaw5685 (2019).
4. Zhang, D. et al. Topological axion states in the magnetic insulator $MnBi_2Te_4$ with the quantized magnetoelectric effect. *Phys. Rev. Lett.* **122**, 206401 (2019).
5. Deng, Y. et al. Quantum anomalous Hall effect in intrinsic magnetic topological insulator $MnBi_2Te_4$. *Science* **367**, 895–900 (2020).
6. Liu, C. et al. Robust axion insulator and Chern insulator phases in a two-dimensional antiferromagnetic topological insulator. *Nat. Mater.* **19**, 522–527 (2020).
7. Wang, N. et al. Quantum-metric-induced nonlinear transport in a topological antiferromagnet. *Nature* **621**, 487–492 (2023).
8. Gao, A. et al. Quantum metric nonlinear Hall effect in a topological antiferromagnetic heterostructure. *Science* **381**, 181–186 (2023).
9. Šmejkal, L., Mokrousov, Y., Yan, B. & MacDonald, A. H. Topological antiferromagnetic spintronics. *Nat. Phys.* **14**, 242–251 (2018).
10. He, Q. L., Hughes, T. L., Armitage, N. P., Tokura, Y. & Wang, K. L. Topological spintronics and magnetoelectronics. *Nat. Mater.* **21**, 15–23 (2022).
11. Chang, C.-Z. et al. Experimental observation of the quantum anomalous Hall effect in a magnetic topological insulator. *Science* **340**, 167–170 (2013).
12. Serlin, M. et al. Intrinsic quantized anomalous Hall effect in a moiré heterostructure. *Science* **367**, 900–903 (2020).

13. Sharpe, A. L. et al. Emergent ferromagnetism near three-quarters filling in twisted bilayer graphene. *Science* **365**, 605–608 (2019).
14. Chen, G. et al. Tunable correlated Chern insulator and ferromagnetism in a moiré superlattice. *Nature* **579**, 56–61 (2020).
15. Li, T. et al. Quantum anomalous Hall effect from intertwined moiré bands. *Nature* **600**, 641–646 (2021).
16. Park, H. et al. Observation of fractionally quantized anomalous Hall effect. *Nature* **622**, 74–79 (2023).
17. Xu, F. et al. Observation of integer and fractional quantum anomalous Hall effects in twisted bilayer $MoTe_2$. *Phys. Rev.* **13**, 031037 (2023).
18. Lu, Z. et al. Fractional quantum anomalous Hall effect in multilayer graphene. *Nature* **626**, 759–764 (2024).
19. Han, T. et al. Large quantum anomalous Hall effect in spin-orbit proximitized rhombohedral graphene. *Science* **384**, 647–651 (2024).
20. Ge, J. et al. High-Chern-number and high-temperature quantum Hall effect without Landau levels. *Natl Sci. Rev.* **7**, 1280–1287 (2020).
21. Ying, Z. et al. Experimental evidence for dissipationless transport of the chiral edge state of the high-field Chern insulator in $MnBi_2Te_4$ nanodevices. *Phys. Rev. B* **105**, 085412 (2022).
22. Cai, J. et al. Electric control of a canted-antiferromagnetic Chern insulator. *Nat. Commun.* **13**, 1668 (2022).
23. Bai, Y. et al. Quantized anomalous Hall resistivity achieved in molecular beam epitaxy-grown $MnBi_2Te_4$ thin films. *Natl Sci. Rev.* **11**, nwad189 (2024).
24. Gao, A. et al. Layer Hall effect in a 2D topological axion antiferromagnet. *Nature* **595**, 521–525 (2021).
25. Zhang, R.-X., Wu, F. & Das Sarma, S. Möbius Insulator and Higher-Order Topology in $MnBi_{2n}Te_{3n+1}$. *Phys. Rev. Lett.* **124**, 136407 (2020).
26. Lei, C., Heinonen, O., MacDonald, A. H. & McQueeney, R. J. Metamagnetism of few-layer topological antiferromagnets. *Phys. Rev. Mater.* **5**, 064201 (2021).
27. Li, Z. et al. Tunable interlayer magnetism and band topology in van der Waals heterostructures of $MnBi_2Te_4$-family materials. *Phys. Rev. B* **102**, 081107 (2020).
28. Sun, H.-P. et al. Analytical solution for the surface states of the antiferromagnetic topological insulator $MnBi_2Te_4$. *Phys. Rev. B* **102**, 241406 (2020).
29. Yang, S. et al. Odd-even layer-number effect and layer-dependent magnetic phase diagrams in $MnBi_2Te_4$. *Phys. Rev.* **11**, 011003 (2021).
30. Sass, P. M., Kim, J., Vanderbilt, D., Yan, J. & Wu, W. Robust *A*-type order and spin-flop transition on the surface of the antiferromagnetic topological insulator $MnBi_2Te_4$. *Phys. Rev. Lett.* **125**, 037201 (2020).
31. Ovchinnikov, D. et al. Intertwined topological and magnetic orders in atomically thin Chern insulator $MnBi_2Te_4$. *Nano Lett.* **21**, 2544–2550 (2021).
32. Garnica, M. et al. Native point defects and their implications for the Dirac point gap at $MnBi_2Te_4$(0001). *npj Quantum Mater.* **7**, 7 (2022).
33. Tan, H. & Yan, B. Distinct magnetic gaps between antiferromagnetic and ferromagnetic orders driven by surface defects in the topological magnet $MnBi_2Te_4$. *Phys. Rev. Lett.* **130**, 126702 (2023).
34. Lai, Y., Ke, L., Yan, J., McDonald, R. D. & McQueeney, R. J. Defect-driven ferrimagnetism and hidden magnetization in $MnBi_2Te_4$. *Phys. Rev. B* **103**, 184429 (2021).
35. Du, M.-H., Yan, J., Cooper, V. R. & Eisenbach, M. Tuning Fermi levels in intrinsic antiferromagnetic topological insulators $MnBi_2Te_4$ and $MnBi_4Te_7$ by defect engineering and chemical doping. *Adv. Funct. Mater.* **31**, 2006516 (2021).
36. Hou, F. et al. Te-vacancy-induced surface collapse and reconstruction in antiferromagnetic topological insulator $MnBi_2Te_4$. *ACS Nano* **14**, 11262–11272 (2020).
37. Huang, Z., Du, M.-H., Yan, J. & Wu, W. Native defects in antiferromagnetic topological insulator $MnBi_2Te_4$. *Phys. Rev. Mater.* **4**, 121202 (2020).
38. Zeugner, A. et al. Chemical aspects of the candidate antiferromagnetic topological insulator $MnBi_2Te_4$. *Chem. Mater.* **31**, 2795–2806 (2019).
39. Li, H. et al. Antiferromagnetic topological insulator $MnBi_2Te_4$: synthesis and magnetic properties. *Phys. Chem. Chem. Phys.* **22**, 556–563 (2020).
40. Li, Y. et al. Fabrication-induced even-odd discrepancy of magnetotransport in few-layer $MnBi_2Te_4$. *Nat. Commun.* **15**, 3399 (2024).
41. Zhang, Z. et al. Controlled large non-reciprocal charge transport in an intrinsic magnetic topological insulator $MnBi_2Te_4$. *Nat. Commun.* **13**, 6191 (2022).
42. Liu, S. et al. Gate-tunable intrinsic anomalous Hall effect in epitaxial $MnBi_2Te_4$ films. *Nano Lett.* **24**, 16–25 (2024).
43. Li, Y. et al. Reentrant quantum anomalous Hall effect in molecular beam epitaxy-grown $MnBi_2Te_4$ thin films. Preprint at arxiv.org/abs/2401.11450 (2024).
44. Wang, Y. et al. Towards the quantized anomalous Hall effect in AlO_x-capped $MnBi_2Te_4$. *Nat. Commun.* **16**, 1727 (2025).
45. Dieny, B. & Chshiev, M. Perpendicular magnetic anisotropy at transition metal/oxide interfaces and applications. *Rev. Mod. Phys.* **89**, 025008 (2017).
46. Monso, S. et al. Crossover from in-plane to perpendicular anisotropy in Pt/CoFe/AlO_x sandwiches as a function of Al oxidation: a very accurate control of the oxidation of tunnel barriers. *Appl. Phys. Lett.* **80**, 4157–4159 (2002).
47. Rodmacq, B., Auffret, S., Dieny, B., Monso, S. & Boyer, P. Crossovers from in-plane to perpendicular anisotropy in magnetic tunnel junctions as a function of the barrier degree of oxidation. *J. Appl. Phys.* **93**, 7513–7515 (2003).
48. Chang, C.-Z. et al. High-precision realization of robust quantum anomalous Hall state in a hard ferromagnetic topological insulator. *Nat. Mater.* **14**, 473–477 (2015).
49. Checkelsky, J. G. et al. Trajectory of the anomalous Hall effect towards the quantized state in a ferromagnetic topological insulator. *Nat. Phys.* **10**, 731–736 (2014).
50. Kou, X. et al. Scale-invariant quantum anomalous Hall effect in magnetic topological insulators beyond the two-dimensional limit. *Phys. Rev. Lett.* **113**, 137201 (2014).
51. Mills, D. L. Surface spin-flop state in a simple antiferromagnet. *Phys. Rev. Lett.* **20**, 18–21 (1968).
52. Bac, S.-K. et al. Topological response of the anomalous Hall effect in $MnBi_2Te_4$ due to magnetic canting. *npj Quantum Mater.* **7**, 46 (2022).
53. Chong, S. K. et al. Intrinsic exchange biased anomalous Hall effect in an uncompensated antiferromagnet $MnBi_2Te_4$. *Nat. Commun.* **15**, 2881 (2024).
54. Bartram, F. M. et al. Real-time observation of magnetization and magnon dynamics in a two-dimensional topological antiferromagnet $MnBi_2Te_4$. *Sci. Bull.* **68**, 2734–2742 (2023).
55. Liu, C. et al. Magnetic-field-induced robust zero Hall plateau state in $MnBi_2Te_4$ Chern insulator. *Nat. Commun.* **12**, 4647 (2021).
56. Luan, J. et al. Controlling the zero Hall plateau in a quantum anomalous Hall insulator by in-plane magnetic field. *Phys. Rev. Lett.* **130**, 186201 (2023).
57. Coey, J. M. D. *Magnetism and Magnetic Materials* (Cambridge Univ. Press, 2010).
58. Chikazumi, S. & Graham, C. D. *Physics of Ferromagnetism* (Oxford Univ. Press, 1997).
59. Silevitch, D. M., Aeppli, G. & Rosenbaum, T. F. Switchable hardening of a ferromagnet at fixed temperature. *Proc. Natl Acad. Sci. USA* **107**, 2797–2800 (2010).
60. Brooke, J., Rosenbaum, T. F. & Aeppli, G. Tunable quantum tunnelling of magnetic domain walls. *Nature* **413**, 610–613 (2001).

Methods

Crystal growth

The $MnBi_2Te_4$ single crystal was grown using the solid-state reaction method. Initially, Mn lump (99.95%, Alfa Aesar) and Te lump (99.999% Alfa Aesar) were mixed in a 1:1 ratio according to the chemical composition. The mixture was ground into powder in an agate mortar, placed into a quartz ampoule and vacuum sealed. The ampoule was slowly heated to 900 °C and maintained at this temperature for 72 h, resulting in the formation of MnTe. Subsequently, the quartz ampoule was removed from the box furnace at 900 °C and quenched in water, yielding MnTe crystals.

Simultaneously, Bi lump (99.999%, 3A) and Te lump (99.999%, Alfa Aesar) were mixed in a 2:3 ratio, ground into powder, placed into a quartz ampoule and vacuum sealed. The ampoule was slowly heated to 800 °C and maintained at this temperature for 6 h, allowing for the uniform mixing of elemental Bi and Te. The temperature was then gradually decreased to 582 °C at a rate of 3 °C min^{-1} and maintained for 4 days. Then, the quartz ampoule was removed from the box furnace and quenched in water, resulting in Bi_2Te_3 crystals.

Subsequently, MnTe, Bi_2Te_3 and elemental Te were mixed in a 1:1:0.2 molar ratio. The mixture was ground into powder in an agate mortar, placed into a quartz ampoule and vacuum sealed. The ampoule was slowly heated to 900 °C at a rate of 3 °C min^{-1} and maintained at this temperature for 1 h, allowing for the uniform melting and mixing of the raw materials. Subsequently, the sample was cooled at a rate of 3 °C min^{-1} to 700 °C, held at this temperature for 1 h. The temperature was then gradually decreased to 585 °C at a rate of 0.5 °C min^{-1} and maintained for annealing for 12 days. After the annealing process, the quartz ampoule was quenched in water to avoid phase impurities. Millimetre-sized $MnBi_2Te_4$ crystals were obtained after crushing the ingot.

Device fabrication

Thin flakes of $MnBi_2Te_4$ were exfoliated using the Scotch tape method onto an Si substrate with 285 nm SiO_2 and pre-cleaned in air plasma for 3 min at approximately 125 Pa pressure. The exfoliation process involved heating at 60 °C for 3 min. The sample thickness was determined by the optical contrast of the photo. Subsequently, a 3-nm layer of aluminium was deposited on the exfoliated samples in a thermal evaporator. Following the deposition, oxygen was introduced into the deposition chamber to maintain a pressure of 2×10^{-2} Pa for 5 min to oxidize aluminium. Then, the surrounding thick layer regions of the flake were removed by a needle. After that, we performed spin-coating of a layer of PMMA resist onto the sample, followed by baking at 60 °C for 7 min. Electrodes were patterned using a standard electron-beam lithography, followed by etching the oxidized aluminium on the top of the sample in an Ar ion milling machine. Metal electrodes (Cr/Au, 3/50 nm) were then deposited using a thermal evaporator connected to a glove box. Finally, the sample was immersed in acetone for the removal of photoresist films. All fabrication processes were conducted in an Ar-filled glove box with O_2 and H_2O levels maintained below 0.1 ppm. During the transfer between the glove box and cryostat, the devices were consistently subjected to spin-coating with a layer of PMMA. Together with the AlO_x layer, it further prevents the air contamination and sample degradation. Acetone, PMMA and isopropyl alcohol used in the fabrication process were all purified with molecular sieves.

First-principles calculation

Density functional theory calculations were performed using Vienna Ab-initio Simulation Package (ref. 61) with the Perdew–Burke–Ernzerhof (PBE) exchange correlational functional[62]. The PBE + U method was used, using U = 4 eV for the 3d orbitals of Mn (ref. 3). The plane-wave energy cutoff of 350 eV and the dense Monkhorst–Pack k-mesh of 30 × 30 × 1 were adopted for calculating the PMA energies. All calculations included the spin–orbit coupling and the DFT-D3 van der Waals corrections[63].

Transport measurements

Transport measurements were conducted in an Oxford dilution refrigerator with vector magnets providing a vertical field up to 9 T and a horizontal field up to 3 T. The excitation current was provided by a Keithley 6221 current source with an excitation of 10 nA at 4.56 Hz. Longitudinal resistance and Hall resistance were measured using standard lock-in technique by NF5650 and NF5645. The back-gate voltage was provided by a Keithley 2400 voltage source.

Data availability

All raw and derived data used to support the findings of this work are available from the authors on request.

61. Kresse, G. & Furthmüller, J. Efficient iterative schemes for *ab initio* total-energy calculations using a plane-wave basis set. *Phys. Rev. B* **54**, 11169–11186 (1996).
62. Perdew, J. P., Burke, K. & Ernzerhof, M. Generalized gradient approximation made simple. *Phys. Rev. Lett.* **77**, 3865–3868 (1996).
63. Grimme, S., Antony, J., Ehrlich, S. & Krieg, H. A consistent and accurate ab initio parametrization of density functional dispersion correction (DFT-D) for the 94 elements H-Pu. *J. Chem. Phys.* **132**, 154104 (2010).

Acknowledgements Yayu Wang was supported the Basic Science Center Project of Natural Science Foundation of China (grant no. 52388201), the Innovation program for Quantum Science and Technology (grant no. 2021ZD0302502) and the New Cornerstone Science Foundation through the New Cornerstone Investigator Program and the XPLORER PRIZE. C.L. was supported by the National Natural Science Foundation of China (grant no. 12274453), Beijing Nova Program (grant no. 20240484574), and the Open Research Fund Program of the State Key Laboratory of Low-Dimensional Quantum Physics (grant no. KF202204). J.Z. was supported by the National Natural Science Foundation of China (grant nos. 12274252 and 12350404) and the National Key Research and Development Program of China (grant no. 2024YFA1409100). We thank W. Wang, S. Yang and H. Yang for their discussions.

Author contributions Yayu Wang, C.L. and J.Z. supervised the research. Z.L., Yongchao Wang, Yongqian Wang, Yaoxin Li, Y.F., B.F. and S.Y. fabricated the devices and performed the transport measurements. Yongchao Wang, L.X. and Yuetan Li grew the $MnBi_2Te_4$ crystals. Z.D. performed the TEM measurements. Z.L., M.M. and W.J. performed the simulation of the spin configurations. W.-H.D. and Y.X. performed the first-principles calculation. Z.L., C.L., J.Z. and Yayu Wang prepared the paper with comments from all authors.

Competing interests The authors declare no competing interests.

Additional information
Supplementary information The online version contains supplementary material available at https://doi.org/10.1038/s41586-025-08860-z.

Correspondence and requests for materials should be addressed to Chang Liu, Jinsong Zhang or Yayu Wang.

Peer review information *Nature* thanks Haijun Zhang and the other, anonymous, reviewer(s) for their contribution to the peer review of this work.

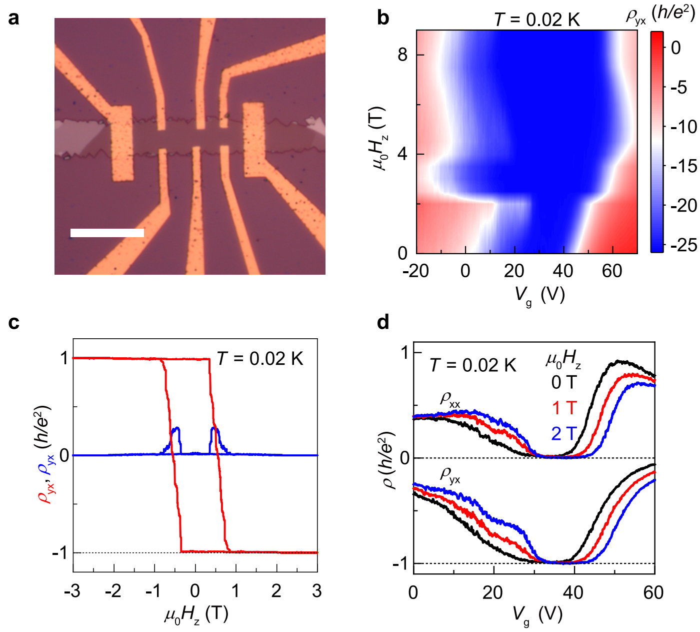

Extended Data Fig. 1 | Transport data of the 7SL $MnBi_2Te_4$ device at T = 0.02 K. **a**, Photograph of the measured device. The scale bar is 10 µm. **b**, Colour map of ρ_{yx} as a function of H_z and V_g at T = 0.02 K. **c**, The μ_0H_z dependent ρ_{xx} (blue) and ρ_{yx} (red) curves at the CNP measured by using the Keithley 6221-2182 in the delta mode with a current of 10 nA and a delay of 0.027 s, which demonstrates ρ_{xx} = 0.012 h/e^2 and ρ_{yx} = 0.988 h/e^2 at μ_0H_z = 0 T. **d**, The evolution of ρ_{xx} and ρ_{yx} as a function of V_g at μ_0H_z = 0, 1, and 2 T.

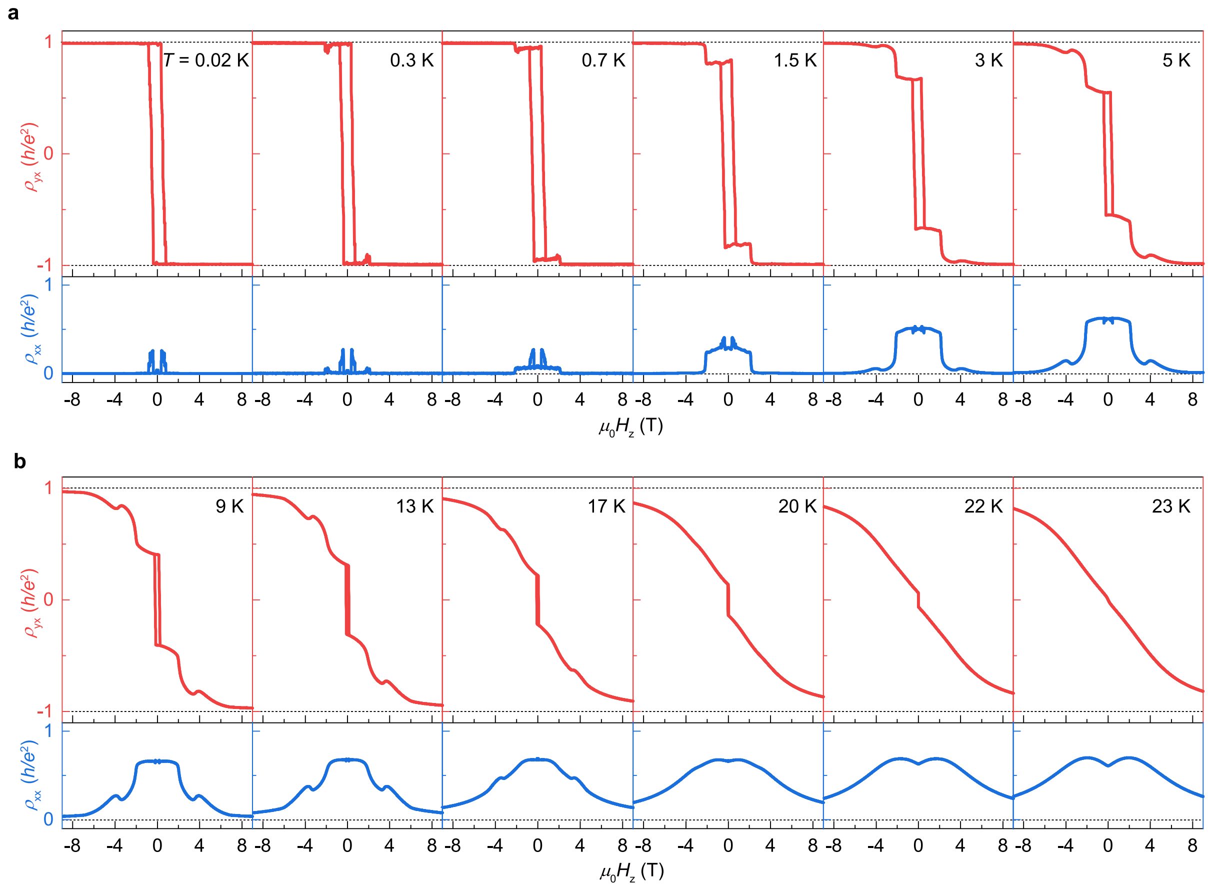

Extended Data Fig. 2 | Individual H_z-dependent ρ_{xx} and ρ_{yx} curves for varied Ts at V_g = 30 V. The upper and lower panels are the ρ_{yx} (red) and ρ_{xx} (blue) curves, respectively, from T = 0.02 K to T = 23 K. The one-step transition in the ground state is replaced by much more complex variations at higher T.

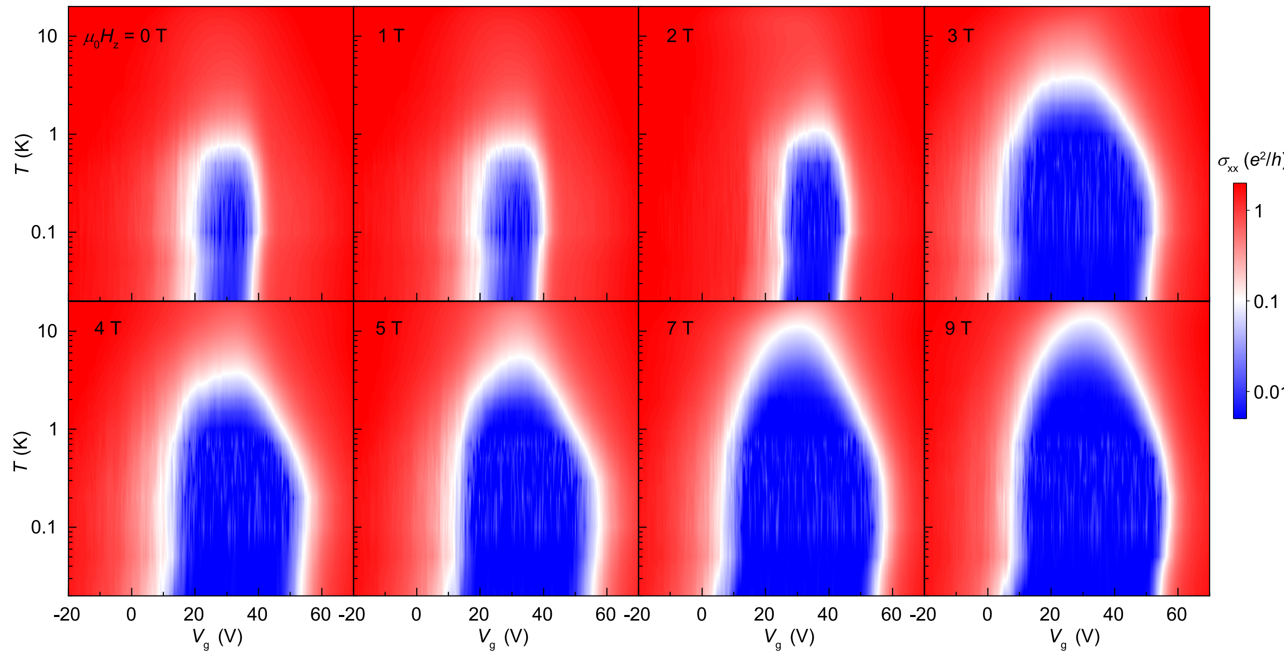

Extended Data Fig. 3 | Colour map of σ_{xx} as a function of T and V_g at various μ_0H_z. The V_g dependent transport data are measured at fixed μ_0H_z and selected Ts (T = 0.02, 0.05, 0.1, 0.2, 0.3, 0.5, 0.7, 1, 1.5, 2, 3, 4, 5, 7, 9, 11, 13, 15, 17 and 20 K). The thermal activation gap size Δ is extracted using the Arrhenius formula $\ln\sigma_{xx} = -\Delta/2k_BT$, where k_B represents the Boltzmann constant.

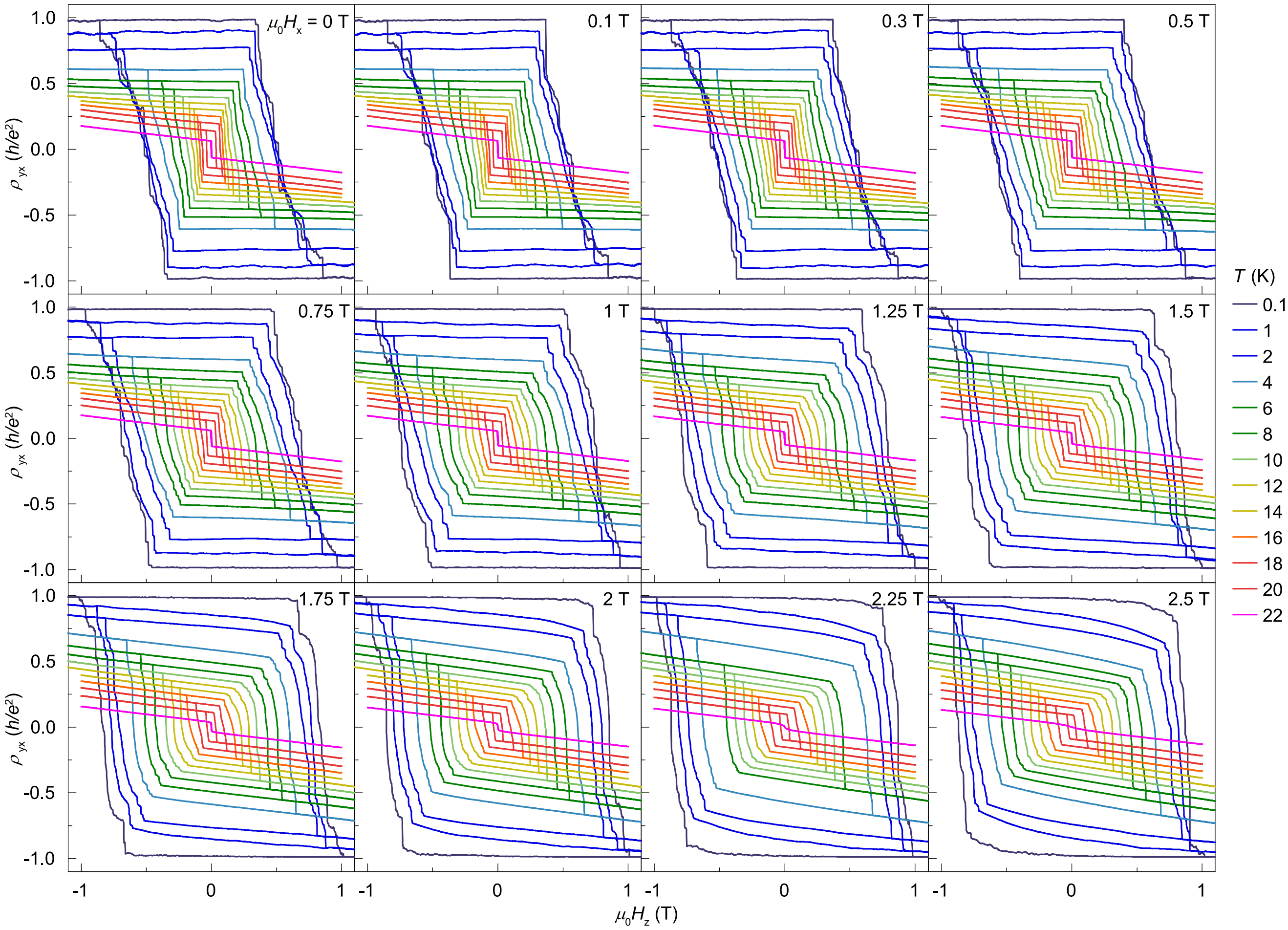

Extended Data Fig. 4 | Complete data of μ_0H_z dependent ρ_{yx} at varied Ts and μ_0H_x. The measurements were conducted by sweeping H_z at different H_x at fixed T. The measuring sequence is from 0.01 K to 22 K. All data taken at V_g = 30 V.

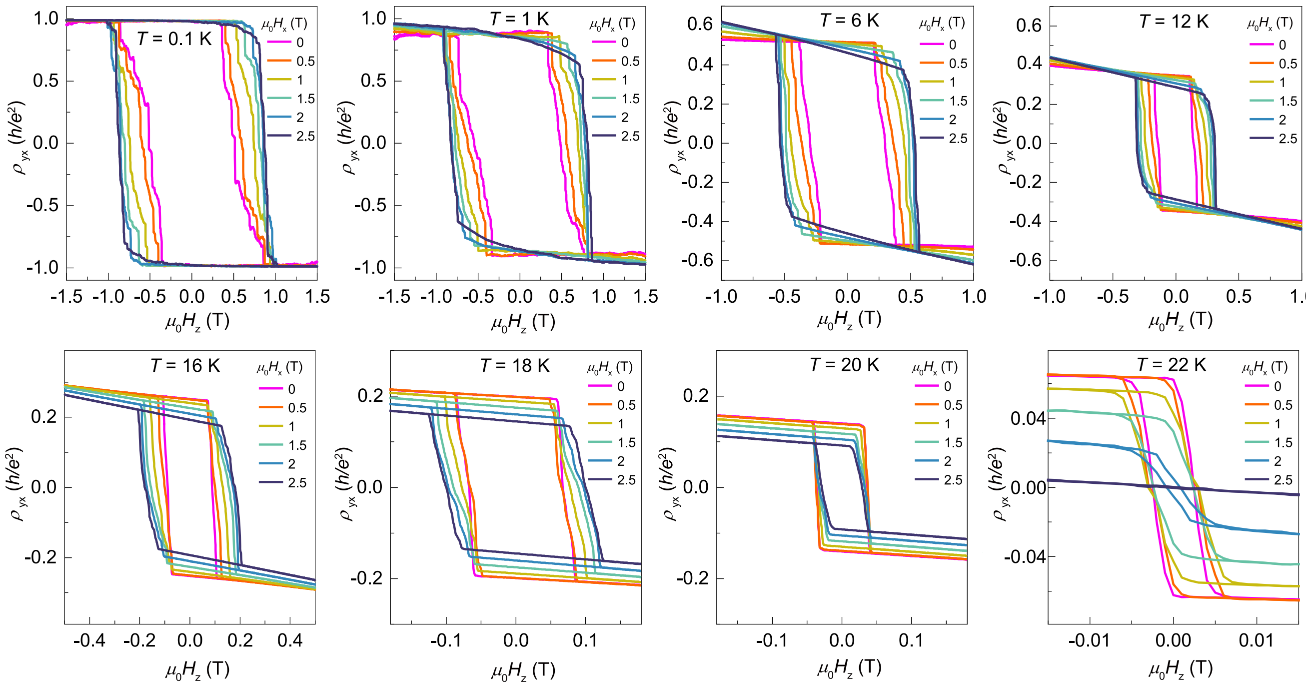

Extended Data Fig. 5 | The hysteresis manipulated by in-plane magnetic field at different *T*s. a-f, The ρ_{yx} versus H_z loops show that the coercivity increases with the application of H_x at $T \leq 18$ K. **g-h**, Near the Néel temperature ($T = 20$ and 22 K), the trend is reversed and the coercivity decreases with the application of H_x. All data taken at $V_g = 30$ V.

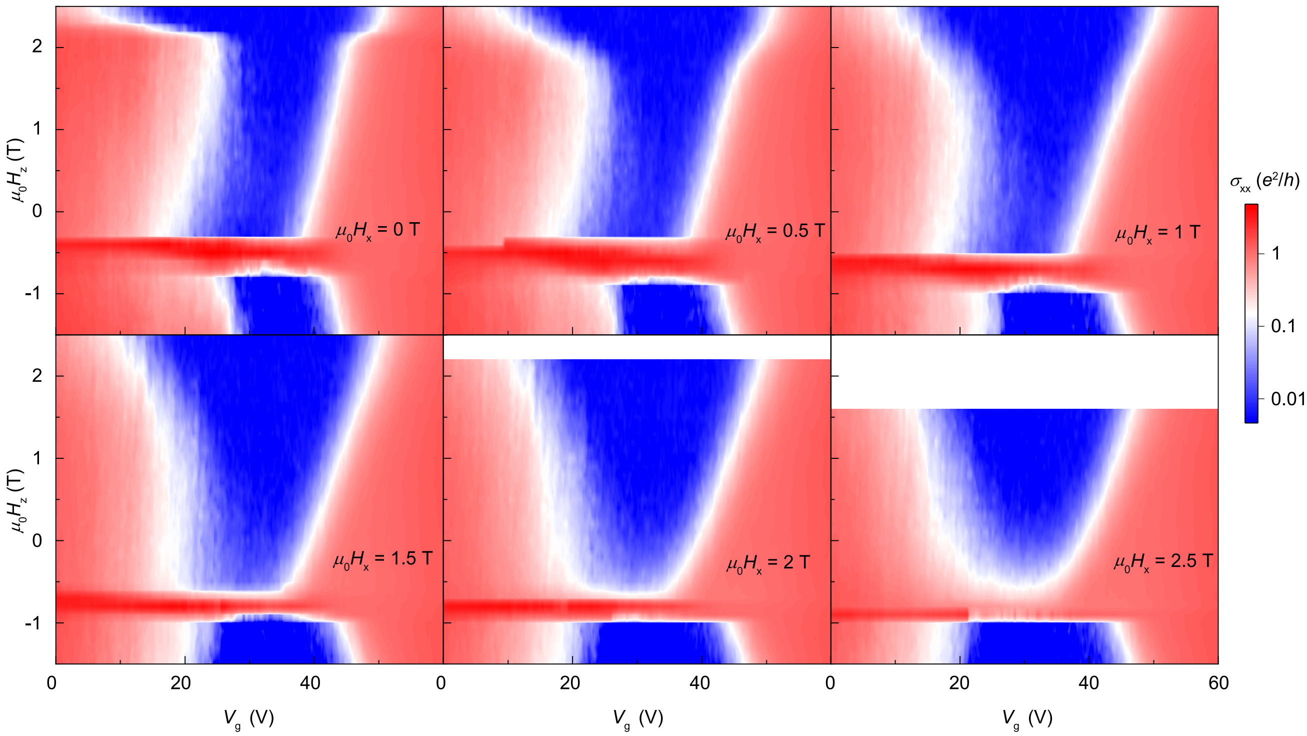

Extended Data Fig. 6 | Colour map of σ_{xx} in the parameter space of μ_0H_z and V_g at T = 0.2 K with increasing μ_0H_x. The measurements were conducted by fixing μ_0H_x and sweeping V_g with μ_0H_z varied from +2.5 T to −1.5 T. As μ_0H_x increases, the QAH region indicated by blue colour is enlarged and the sudden gap increase at $\mu_0H_z \approx 2.2$ T becomes smoother. When μ_0H_x is increased to 2 T, the AFM to SSF transition nearly disappears.

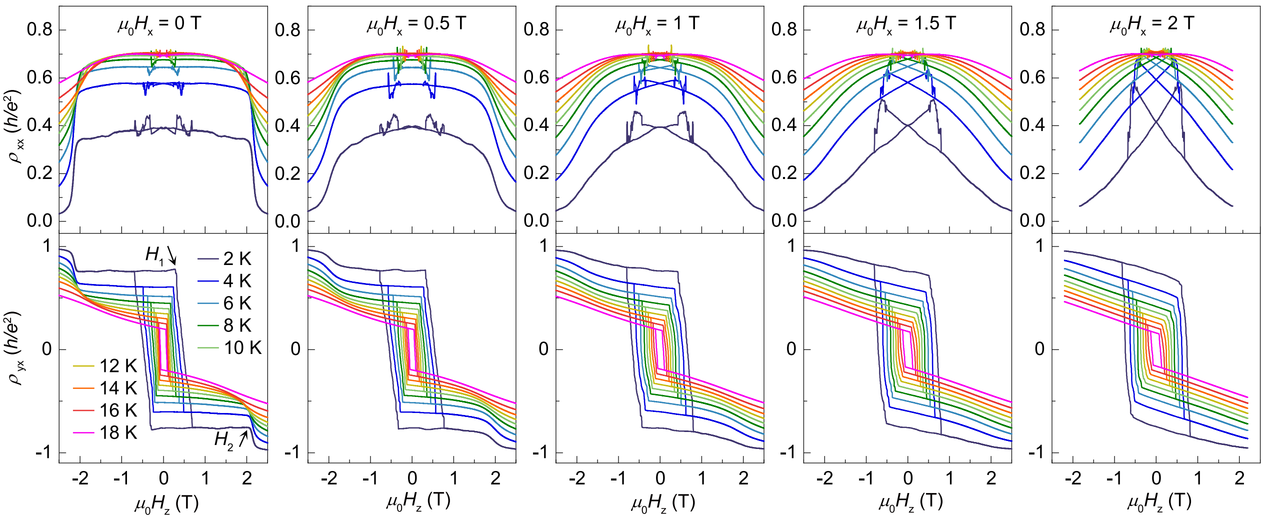

Extended Data Fig. 7 | The μ_0H_z dependence of ρ_{xx} and ρ_{yx} at varied μ_0H_x. The application of H_x smears out the transition at H_2 in both ρ_{xx} (upper panel) and ρ_{yx} (lower panel). Meanwhile, the hysteresis is increased, accompanied by a sharper transition at H_1. All data taken at V_g = 30 V.